Fluid–structure interaction and flow sensing of primary cilia in oscillating fluid flows ⊘

Jingyu Cui ⓘ ; Yuzhen Jin ✉ ⓘ ; Yang Liu ✉ ⓘ ; Bingmei M. Fu ⓘ ; Weiwei Yan

Check for updates

View Online   Export Citation

Articles You May Be Interested In

Measurement of fluid flow generated by artificial cilia

Biomicrofluidics (July 2011)

Symmetry Breaking in a Model for Nodal Cilia

AIP Conference Proceedings (March 2005)

A microfluidic device for *in situ* fixation and super-resolved mechanosensation studies of primary cilia

Biomicrofluidics (January 2019)

13 January 2025 02:40:17

AIP Publishing

Physics of Fluids

Special Topics Open for Submissions

Learn More

AIP Publishing

Fluid–structure interaction and flow sensing of primary cilia in oscillating fluid flows

View Online   Export Citation   CrossMark

Jingyu Cui,[1] (iD) Yuzhen Jin,[1,a)] (iD) Yang Liu,[2,a)] (iD) Bingmei M. Fu,[3] (iD) and Weiwei Yan[4]

AFFILIATIONS

[1]Key Laboratory of Fluid Transmission Technology of Zhejiang Province, Zhejiang Sci-Tech University, Hangzhou 310018, China
[2]Research Centre for Fluid-Structure Interactions, Department of Mechanical Engineering, The Hong Kong Polytechnic University, Hung Hom, Hong Kong
[3]Department of Biomedical Engineering, City College of New York, New York, NY 10031, USA
[4]College of Metrology and Measurement Engineering, China Jiliang University, Hangzhou 310018, China

[a)]Authors to whom correspondence should be addressed: gracia1101@foxmail.com and mmyliu@polyu.edu.hk

ABSTRACT

This study systematically investigates the interaction between an oscillating flow and primary cilia using numerical simulations. The primary cilia are modeled as elastic filaments with rotatable basal ends to mimic real ciliary deflections. How some governing parameters [i.e., the peak Reynolds number (Re_{peak}), Womersley number (Wo), cilium length (L^*), and streamwise spacing interval (L_d^*)] regulate fluid–cilia interaction is explored. Our results indicate that within a certain range, both the span of deflection (SD) and the maximal curvature increase with the increase in Re_{peak}, L^*, and L_d^*, while they decrease as the Wo increases. Compared with other parameters, L_d^* affects ciliary deflection less significantly and its impact becomes nearly negligible when the cilia are separated over twice their length. Three typical stretch states are captured. For primary cilia with a short or medium length, an increase in the SD is accompanied by a greater propagation distance of the location of the maximal tensile stress (LMTS). However, this is not the case for long cilia that protrude into 1/3 of the lumen, as the arising third stretch state may greatly suppress the LMTS propagation. Our study further confirms the role of primary cilia in decreasing the wall shear stress (WSS) and altering its oscillating feature. The WSS decrease is more significant for cilia undergoing a larger SD and/or when L_d^* is reduced. For a constant L_d^*, a larger SD corresponds to a more uneven oscillatory shear index distribution, and the affected (i.e., less oscillatory) region appears to greatly depend on L_d^*.

Published under an exclusive license by AIP Publishing. https://doi.org/10.1063/5.0140701

I. INTRODUCTION

Primary cilia are filamentous, nonmotile surface extensions that can be found in nearly every mammalian cell.[1,2] The exact functions of primary cilia are still not fully understood although they were first discovered over a century ago when they were regarded as vestigial organelles.[3] Nowadays, increasing evidence shows that primary cilia work as flow sensors[4–7] and they play a vital role in maintaining the functions and homeostasis of cells and tissues in mammals.[8] Deflection of primary cilia is known to initiate the operation of a variety of signaling cascades,[4–7] and primary cilia with impaired ciliary protein or physical structure could lead to numerous diseases known as ciliopathies, e.g., polycystic kidney disease,[9,10] cystic and fibrotic liver disease,[11] osteoarthritis,[12] obesity,[13] and even cancer.[14,15]

A plenty of experimental studies have been conducted to address the mechanosensing mechanism of primary cilia from a biological point of view, with many of them trying to reveal the

mechanical properties of primary cilia as well as the detailed functions of these signaling pathways. From a biomechanics viewpoint, the way how the primary cilia respond to a time-varying hydrodynamic input is crucial for their sensing activities and functions. Understanding the flow sensing characteristics of primary cilia may greatly enrich our knowledge of primary cilia as sensory organelles. However, until now, this aspect still remains largely under-explored with many key questions not been answered. For example, the primary cilia are reported to dynamically regulate their mechanosensitive response by changing their length and bending stiffness.[16–18] How do the mechanical properties of primary cilia impact their sensing ability and characteristics? Different flow strengths will lead to different ciliary deflections. How do they map to each other? The PC2 cation channel localizing to the ciliary membrane is believed to be stretch-activated.[6,7] How will stress and strain be distributed on the ciliary membrane when a primary cilium gets dynamically

13 January 2025 02:40:17

deflected? In pulsatile or oscillatory flow conditions, will primary cilia give a real-time or delayed response? As flow sensors, what is the impact of primary cilia on the surrounding flow field? On the other hand, the flow-induced deflection of an anchored deformable filament is a typical fluid–structure interaction (FSI) problem. A study on this problem not only has important academic value but also has rich practical implications. For instance, it may shed light on the design of bio-inspired flow sensors which can be used to reflect or measure the near-wall flow structures.

Typical reported length of endothelial primary cilia ranges from 0.5 to 15 μm,[19] while the diameter is about 0.2 μm.[20] It is difficult to experimentally qualify the force and stress during the mechanotransduction process in such small scales, and numerical simulations, which provide much more detailed information, can be useful in studying the complex fluid–cilia interaction system. In this study, direct numerical simulations are performed to systematically investigate the FSI of primary cilia in a 3D oscillating flow. The fluid–cilia interaction is resolved by the immersed boundary-lattice Boltzmann method, and the primary cilium is modeled as a flexible filament whose basal end is attached to a nonlinear rotational spring to reproduce the ciliary basal rotation captured in previous experiments.[21–23] The primary focus of this paper is to address how the governing parameters of the system regulate the flow sensing of primary cilia via flow-mediated interaction.

II. PHYSICAL MODEL AND NUMERICAL METHOD

A. Problem description

Figure 1 gives a schematic view of the considered problem. The simulation box has a dimension of $L_d \times W_d \times H_d$. The primary cilium anchors at the center of the bottom plate, initially stands up straight with zero velocity, and is unstressed. The flow is assumed to be periodic in both the x- and y- directions. The bottom plate is imposed with the no-slip boundary condition, and the top plate with the symmetry boundary condition. With these settings, we are able to study the dynamics of two face-to-face placed and synchronous cilia arrays with the minimum computational load. It is also assumed that the flow is incompressible, laminar, Newtonian, and oscillating. To characterize the flow, we define the peak Reynolds number (Re_{peak}) and the Womersley number (Wo) as

$$Re_{peak} = \frac{u_0 D}{v}, \quad Wo = D\sqrt{\frac{2\pi f}{v}}, \quad (1)$$

where $D = 2H_d$ is the separation distance between the upper and bottom plates where the cilia arrays anchor. f is the oscillation cycle, and u_0 is the maximal flow speed that can be obtained during an oscillation.

The oscillation of the flow is generated by applying a sinusoidal pressure gradient waveform as follows:
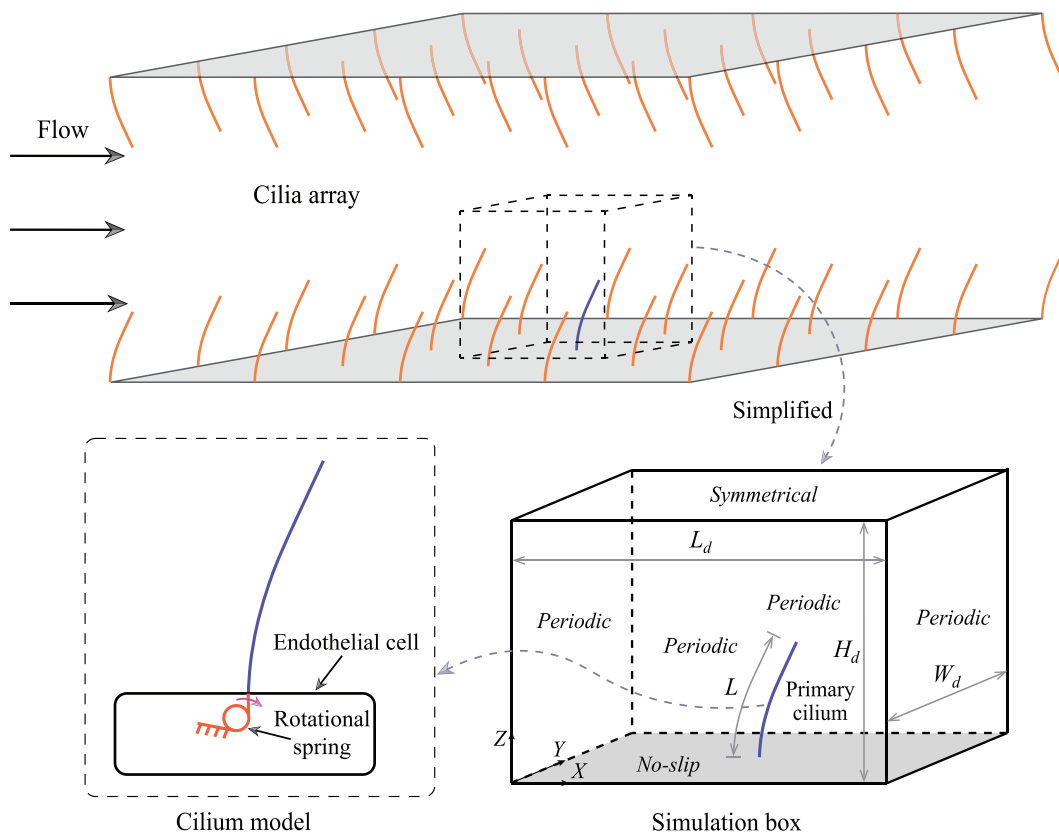

FIG. 1. Schematics of the considered problem.

$$\frac{dp}{dx} = A \sin(2\pi f t), \qquad (2)$$

where t is the time, and $A = 8\rho u_0 v / D^2$ is the amplitude of the waveform.

The following non-dimensionalization is introduced in this study:

$$L^* = \frac{L}{D}, \quad L_d^* = \frac{L_d}{L'}, \quad W_d^* = \frac{W_d}{L'}, \qquad (3)$$

where $L' = 6\,\mu m$ is the reference cilium length and the quantities with asterisk denote their non-dimensional counterparts.

In this study, Re_{peak} and Wo are specified first and then the peak pressure gradient and oscillation frequency f are determined and used as input for the simulations. As our current study focuses on the cilia array in relatively narrow lumens, the physiologically relevant Re_{peak} and Wo chosen here are relatively small, indicating that the flow viscous effects dominate over its inertial and pulsatile effects. The basic parameters of this fluid–cilium coupling system can be found in Table I.

B. Cilium model

The primary cilium in this study is modeled as a flexible filament (i.e., a space curve) owing to its large aspect ratio (Fig. 1). Its motion is governed by the following equation[24–27] (for clarification, hereafter, we will use lowercase variables for the fluid dynamics and uppercase variables for the structure dynamics):

$$\rho_d \frac{\partial^2 \mathbf{X}}{\partial t^2} = \frac{\partial}{\partial s}\left[T(s) \frac{\partial \mathbf{X}}{\partial s} \right] - K_b \frac{\partial^4 \mathbf{X}}{\partial s^4} + \mathbf{F_{fluid}}, \qquad (4)$$

where $\mathbf{X}$ is the position vector of the filament, and s is the Lagrangian coordinate along the arc. K_b is the bending rigidity of the primary cilium, and ρ_d is the linear density difference between the cilium and the fluid. $\mathbf{F_{fluid}}$ is the hydrodynamic force exerted on the cilium, which is evaluated using a force-corrected direct-forcing method.[28] $T(s)$ is the

TABLE I. Basic parameters used in the simulations.

Parameter	Symbol	Value
Length ratio	L^*	1/6, 1/4, and 1/3
Cilium diameter	d	$0.2\,\mu m$ (Ref. 20)
The height of the computational domain	H_d	$12\,\mu m$
x-spacing interval (dimensionless)	L_d^*	0.5, 1.0, 2.0, and 3.0
y-spacing interval (dimensionless)	W_d^*	0.6
Fluid density	ρ_f	$1000\,kg/m^3$
Cilium density	ρ_c	$1110\,kg/m^3$ (Ref. 18)
Fluid kinematic viscosity	v	$1.2 \times 10^{-6}\,m^2/s$
Bending rigidity of cilium	K_b	$1.5 \times 10^{-23}\,Nm^2$
Linear spring constant	k	$4.6 \times 10^{-12}\,N/rad$ (Ref. 23)
Nonlinear spring constant	α	$-1 \times 10^{-10}\,N/rad^2$ (Ref. 23)
Peak Reynolds number	Re_{peak}	0.05, 0.1, 0.2, 0.3, and 0.4
Womersley number	Wo	0.4, 0.6, 0.8, 1.0, 1.2, and 1.4

tension. In this method, a local adjustment parameter $\lambda(\mathbf{X}, t)$ is introduced to well enforce the no-slip condition at the fluid–solid interface so that nonphysical streamline penetration[29,30] can be avoided,

$$\mathbf{F_{fluid}}(\mathbf{X}, t) = -2\lambda(\mathbf{X}, t)\rho \frac{\mathbf{U}_b(\mathbf{X}, t) - \mathbf{U}_b^*(\mathbf{X}, t)}{\Delta t}, \qquad (5)$$

where $\mathbf{U}_b(\mathbf{X}, t)$ and $\mathbf{U}_b^*(\mathbf{X}, t)$ are the desired and could-be boundary velocities of the filament, respectively. In our code implementation, $\mathbf{U}_b^*(\mathbf{X}, t)$ is obtained via interpolation on the unforced flow velocity $\mathbf{u}^*(\mathbf{x}, t)$,

$$\mathbf{U}_b^*(\mathbf{X}, t) = \sum_{\mathbf{x}} \mathbf{u}^*(\mathbf{x}, t)\delta(\mathbf{x} - \mathbf{X})h^3, \qquad (6)$$

where δ is the Dirac delta function,[31] and h is the spacing of the Eulerian (fluid) grid.

The primary cilium is discretized by N Lagrangian points $\mathbf{X}(s_n, t)$, $n = 0, 1, \ldots, N-1$, which have a uniform spacing Δs. For Lagrangian point $\mathbf{X}(s_n, t)$, its corresponding λ_n value is explicitly determined using the following equation:

$$\lambda_n = \frac{1}{\Delta s h^5 \sum_{i,j,k} \sum_m \delta(\mathbf{x}_{i,j,k} - \mathbf{X}_m)\delta(\mathbf{x}_{i,j,k} - \mathbf{X}_n)}, \qquad (7)$$

where i, j, and k are the fluid point indexes. A more detailed implementation of the force-corrected direct-forcing method can be found in Ref. 28. The stretching and bending force terms in Eq. (4) are approximated by a central finite difference stencil,

$$\frac{\partial}{\partial s}\left[T(s) \frac{\partial \mathbf{X}}{\partial s} \right] = \frac{\left[T(s)\frac{\partial \mathbf{X}}{\partial s} \right]_{n+\frac{1}{2}} - \left[T(s)\frac{\partial \mathbf{X}}{\partial s} \right]_{n-\frac{1}{2}}}{\Delta s}$$

$$= \frac{T_{n+\frac{1}{2}}(\mathbf{X}_{n+1} - \mathbf{X}_n) - T_{n-\frac{1}{2}}(\mathbf{X}_n - \mathbf{X}_{n-1})}{\Delta s^2}, \qquad (8)$$

$$K_b \frac{\partial^4 \mathbf{X}}{\partial s^4} = K_b \frac{\mathbf{X}_{n+2} - 4\mathbf{X}_{n+1} + 6\mathbf{X}_n - 4\mathbf{X}_{n-1} + \mathbf{X}_{n-2}}{\Delta s^4}, \qquad (9)$$

where Δs is the spacing of the Lagrangian (structure) grid. The tension $T(s)$ is defined as

$$T(s) = K_s \left[\left(\frac{\partial \mathbf{X}}{\partial s} \cdot \frac{\partial \mathbf{X}}{\partial s} \right)^{\frac{1}{2}} - 1 \right]. \qquad (10)$$

In this study, we evaluated $T(s)$ at the segment center (i.e., $n+\frac{1}{2}$, $n = 0, 1, \ldots, N\text{-}1$) with a central difference scheme,

$$T_{n+\frac{1}{2}} = K_s \left(\left| \frac{\mathbf{X}_{n+1} - \mathbf{X}_n}{\Delta s} \right| - 1 \right) \quad \text{and} \quad T_{n-\frac{1}{2}} = K_s \left(\left| \frac{\mathbf{X}_n - \mathbf{X}_{n-1}}{\Delta s} \right| - 1 \right), \qquad (11)$$

where K_s is a stretching coefficient that enforces the inextensibility condition of the cilium.

With the forces on the right-hand side of Eq. (4) obtained, the position and velocity of the cilium are then updated using a third-order Runge–Kutta method due to its improved stability.[32] To reproduce the experimentally observed basal rotations of primary cilium,[21,22] we follow Resnick[23] to model the basal end as a nonlinear

rotational spring while setting the distal end free (Fig. 1). In that case, the boundary conditions at the two end points become

For the distal end ($s = L$):

$$\frac{d^2 X}{ds^2} = \frac{d^3 X}{ds^3} = 0, \tag{12}$$

For the basal end ($s = 0$):

$$X = X_0 \quad \text{and} \quad \frac{d^2 X}{ds^2} = \frac{L}{K_b}\left[k\frac{dX}{ds} + \alpha\left(\frac{dX}{ds}\right)^2 \right], \tag{13}$$

where k and α are the linear and nonlinear spring constants. Equation (12) ensures that the moment and transverse stress vanish at the distal end, and Eq. (13) means that a basal rotation induced by the hydrodynamic load will generate a reverse bending moment at the end.

C. Flow dynamics

The flow dynamics is described by the following governing equations:

$$\nabla \cdot u = 0, \tag{14}$$

$$\rho\left(\frac{\partial u}{\partial t} + u \cdot \nabla u\right) = -\nabla p + \mu \Delta u + f_e, \tag{15}$$

where u is the flow velocity, ρ is the flow density, and μ is the dynamic viscosity of the fluid. p is the pressure, and f_e is the boundary force from the primary cilium. This body force is used in the immersed boundary method (IBM)[31,33–37] to model the boundary impact on the fluid flow. In the IBM, the fluid feels the existence of the immersed structure by inserting such a body force into the momentum equations, and the immersed structure is forced to move and/or deform to enforce the no-slip condition at the boundary.

The flow dynamics in this study is solved by the multi-relaxation-time (MRT) lattice Boltzmann method (LBM) with a D3Q19 lattice model. For more details of this lattice model, interested readers are referred to Ref. 38. In the MRT-LBM, the collision step is performed in the moment space and the moments relax to their equilibria at their own rates. In this way, the solution will be viscosity independent and the simulation will be more stable.[39] Hereafter, we will use the notation $|\cdot\rangle$ to denote column vectors. The evolution equation of the MRT-LBM with Guo's split forcing scheme is given as[40]

$$|f(x + e_\alpha \Delta t,\ t + \Delta t)\rangle - |f(x,\ t)\rangle$$
$$= -M^{-1}\left\{ \hat{S}\left[|m(x,\ t)\rangle - |m^{eq}(x,\ t)\rangle\right] + \left(I - \frac{\hat{S}}{2}\right)|F(x,\ t)\rangle \right\}, \tag{16}$$

where $f(x,\ t)$ is the particle density distribution function. $m(x,\ t)$ is the moment form of $f(x,\ t)$, and $m^{eq}(x,\ t)$ is its equilibrium value. They are defined as

$$|m\rangle = (\rho,\ e,\ \varepsilon,\ j_x,\ j_y,\ q_x,\ j_y,\ q_y,\ j_z,\ q_z,\ 3p_{xx},\ 3\pi_{xx},\ p_{ww},$$
$$\pi_{ww},\ p_{xy},\ p_{yz},\ t_x,\ t_y,\ t_z)^T, \tag{17}$$

$$|m^{eq}\rangle = \left(\rho,\ -\rho(11 - 19|u|^2),\ \rho(3 - 5.5|u|^2),\ j_x,\ -\frac{2}{3}j_x,\ j_y,\right.$$
$$-\frac{2}{3}j_y,\ j_z,\ -\frac{2}{3}j_z,\ \frac{1}{\rho_0}\left(j_x^2 - j_y^2 - j_z^2\right),\ \frac{-1}{2\rho_0}\left(j_x^2 - j_y^2 - j_z^2\right),$$
$$\left. \frac{1}{\rho_0}\left(j_y^2 - j_z^2\right),\ \frac{\gamma}{\rho_0}\left(j_y^2 - j_z^2\right),\ \frac{1}{\rho_0}j_x j_y,\ \frac{1}{\rho_0}j_y j_z,\ \frac{1}{\rho_0}j_z j_x,\ 0,\ 0,\ 0\right)^T. \tag{18}$$

A detailed description on what moments these symbols represent can be found in Ref. 38.

M is a 19×19 transformation matrix, which defines the mapping between f and m, i.e., $|m\rangle = M|f\rangle$. $\hat{S}$ is the non-negative diagonal collision matrix, which is given as follows:

$$\hat{S} \equiv \text{diag}\{1,\ s_1,\ s_2,\ 1,\ s_4,\ 1,\ s_4,\ 1,\ s_4,\ s_9,\ s_{10},\ s_9,$$
$$s_2,\ s_{13},\ s_{13},\ s_{13},\ s_{16},\ s_{16},\ s_{16}\}, \tag{19}$$

where $s_1 = 1.19$, $s_2 = 1.4$, $s_4 = 1.2$, $s_{16} = 1.98$, and $s_9 = s_{13} = 1/(3\nu + 0.5)$, where ν is the kinetic viscosity of the fluid.

$|F(x, t)\rangle$ in Eq. (16) is the force term, which is calculated by[41,42]

$$|F(x, t)\rangle = M|f_e(x, t)\rangle = \frac{[e_\alpha - u(x,\ t)]f_e(x,\ t)}{\rho c_s^2} M|f^{eq}(x,\ t)\rangle, \tag{20}$$

where $f^{eq}(x,\ t)$ is the equilibrium distribution function, and the external force $f_e(x,\ t)$ is obtained via spreading the reaction force of F_{fluid} to the nearby fluid points,

$$f_e(x,\ t) = -\sum_X F_{fluid}(X, t)(x - X)\Delta s. \tag{21}$$

III. RESULTS AND DISCUSSION

The simulations are run by our in-house code which is well validated and verified in our previous studies.[43,44] As a follow-up study, here, we explore the fluid–cilium system more systematically by considering the effect of broader parameters. Specifically, the following four key governing parameters are covered:

(1) Peak Reynolds number (Re_{peak})
The Re_{peak} is varied by varying the amplitude of the waveform (A). As we focus on the fluid–cilium system in relatively small lumens in this study, the physiologically relevant Re_{peak} is chosen as 0.05, 0.1, 0.2, 0.3, and 0.4, respectively. Other parameters are fixed, and their values are given as $Wo = 0.6$, $L^* = 1/4$, $L_d^* = 2.0$, and $W_d^* = 0.8$.

(2) Womersley number (Wo)
The Wo expresses the ratio of the oscillatory inertia force to the viscous force. In different types of human blood vessels, this number varies significantly due to the variations in vessel size across the vasculature system. Based on the lumen size, Wo of 0.4, 0.6, 0.8, 1.0, 1.2, and 1.4 is considered, and varying of Wo is achieved by altering the oscillating frequency f in Eq. (1). Other parameters are fixed at the values of $Re_{peak} = 0.2$, $L^* = 1/4$, $L_d^* = 1.5$, and $W_d^* = 0.6$.

(3) Length ratio (L^*)
The primary cilium is reported to regulate its mechanosensitive response via dynamically changing its length.[16–18] Therefore, the impact of L^* (which characterizes how much the cilium

extends into the lumen) on the fluid–cilium system is also examined. Our current study considered three different length ratios, i.e., $L^* = 1/6$, 1/4, and 1/3, which represent short, medium, and long cilium, respectively. Other parameters are chosen as $Re_{peak} = 0.2$, $Wo = 0.6$, $L_d^* = 2.0$, and $W_d^* = 0.8$.

(4) Spacing interval in the flow direction (L_d^*)

The impact of L_d^* on the fluid–cilium system was also investigated (the spacing interval in the y-direction W_d^* has a far less significant impact on the system, and thus, it is not considered in this study). L_d^* is set as 0.5, 1.0, 2.0, and 3.0, respectively, in this part of simulations with the other parameters being $Re_{peak} = 0.2$, $Wo = 0.6$, $L^* = 1/4$, and $W_d^* = 0.8$. A smaller L_d^* means a denser cilia array in the x-direction, while a larger L_d^* denotes a sparser cilia arrangement.

A. Cilium deflection

Figure 2 shows the simulated superpositions of the cilium profiles for different cases, and Fig. 3 plots the cilium's maximal height and deflection as a function of the Re_{peak}, Wo, L^*, and L_d^*, respectively. The superpositions are found to be symmetrical in all the simulated cases. From Figs. 2(a) and 3(a), we can see that the span of deflection (SD, i.e., twice the maximal deflection) increases with the Re_{peak} and the cilium behaves more complaint at a higher Re_{peak}. This is intuitive as the flow drag increases with the Re_{peak}. However, the increasing rate of the SD is found to decrease with the Re_{peak}, suggesting that there exists an upper limit for the SD, which is independent of the applied Re_{peak}. Increasing the Wo, however, is found to decrease the SD, and the cilium will behave stiffer [Figs. 2(b) and 3(b)]. The curve tends to be flatter at both ends, which indicates that the cilium becomes insensitive
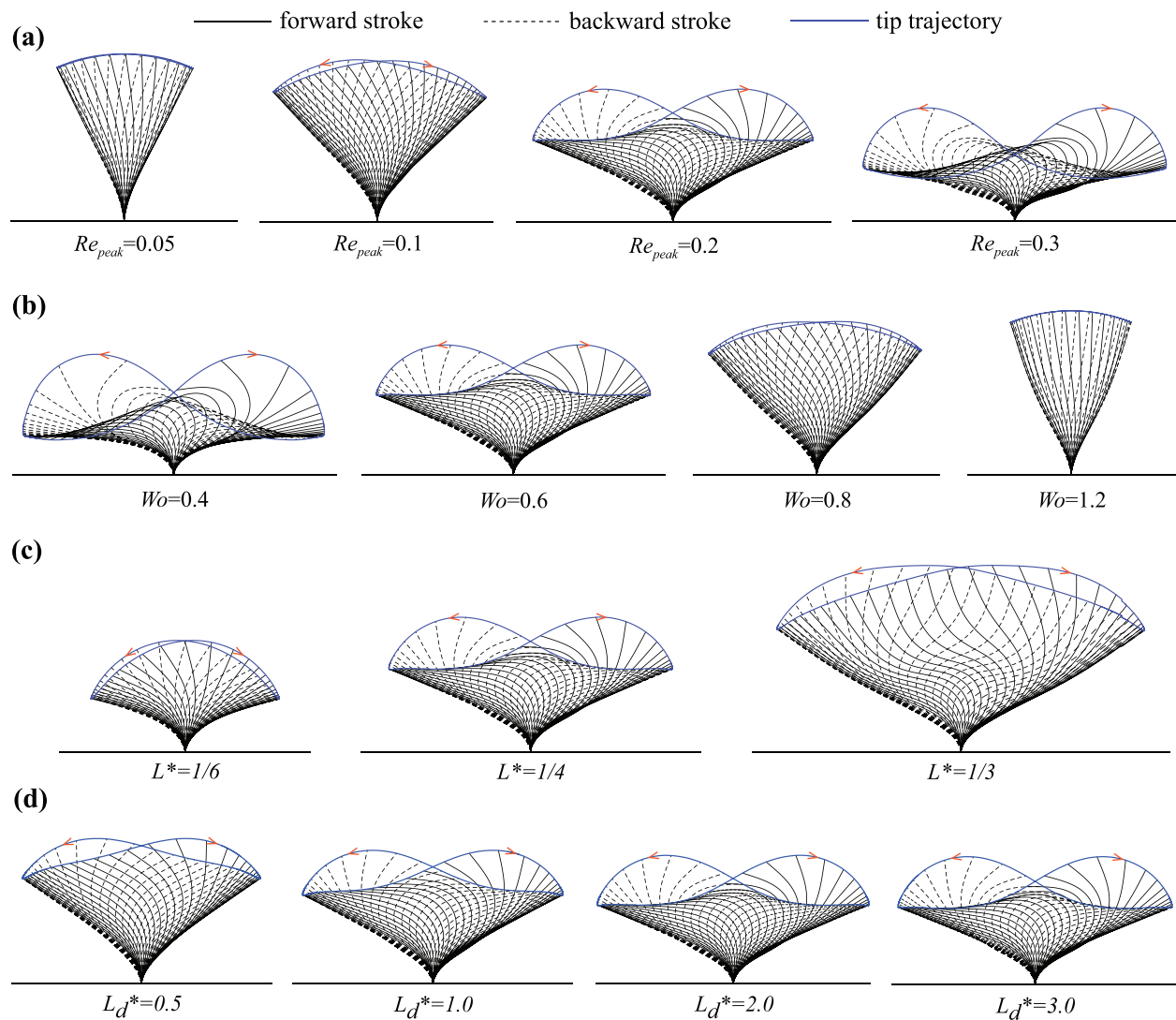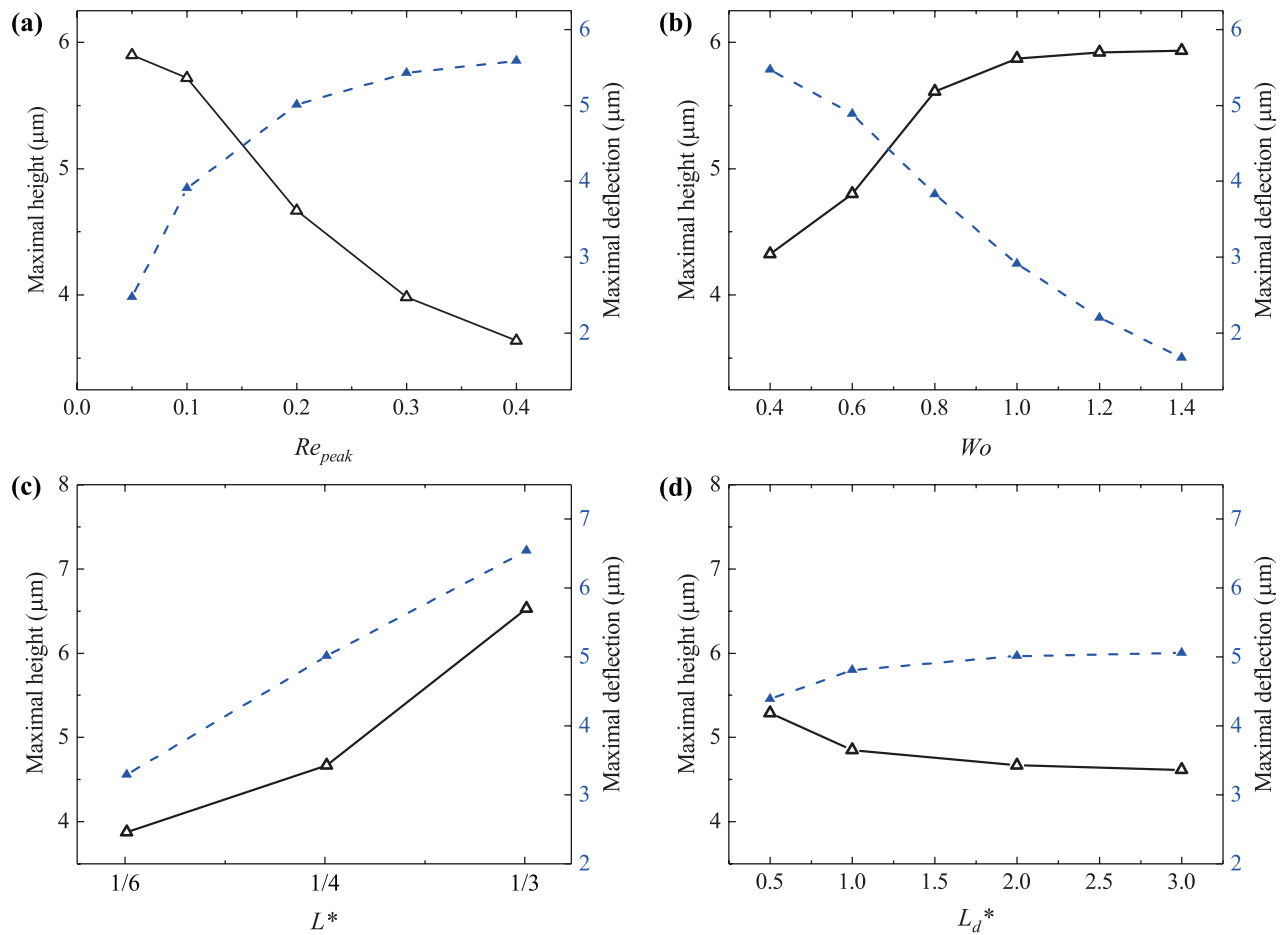

FIG. 2. Simulated superpositions of the cilium profiles for various governing parameters: (a) Re_{peak}, (b) Wo, (c) L^*, and (d) L_d^*.

FIG. 3. Maximal cilium height and deflection as a function of the (a) Re_{peak}, (b) Wo, (c) L^*, and (d) L_d^*. The dashed blue lines represent the maximal deflection with the scale shown at the right axis.

to the Wo of both low and high ranges. An increase in the L^* can also bring a larger SD and more distorted cilium profiles [Figs. 2(c) and 3(c)]. By protruding more into the lumen (i.e., increasing L^*), the primary cilium is able to collect more flow information and simultaneously, it will be exposed to a larger hydrodynamic load and thus deflects more significantly. Therefore, increasing the length of primary cilium may also help to amplify the flow signal when the ambient flow strength is weak (e.g., when senses a flow of

low flow rate). By making the cilia array sparser (i.e., increasing the L_d^*), the SD could also get slightly increased [Fig. 3(d)]. However, this increase is only found for relatively denser cilia arrays whose L_d^* is smaller than twice the cilium length ($L_d^* \leq 2$). Once the L_d^* goes beyond that range, further increasing the L_d^* would almost make no difference to the superposition [Fig. 2(d)]. From Fig. 2, we can see that when the SD is large enough, the tip trajectory forms an eight-shaped loop. According to Fig. 3, an increase in the
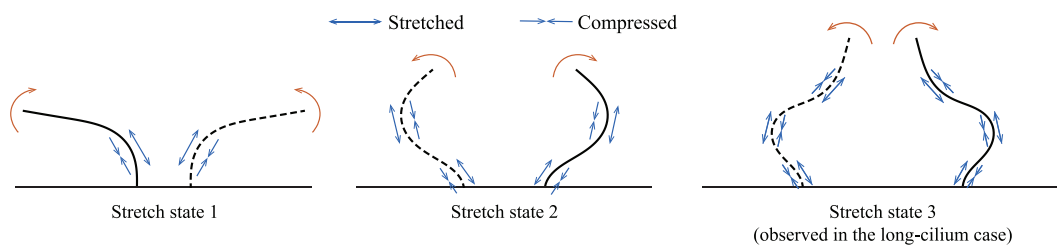
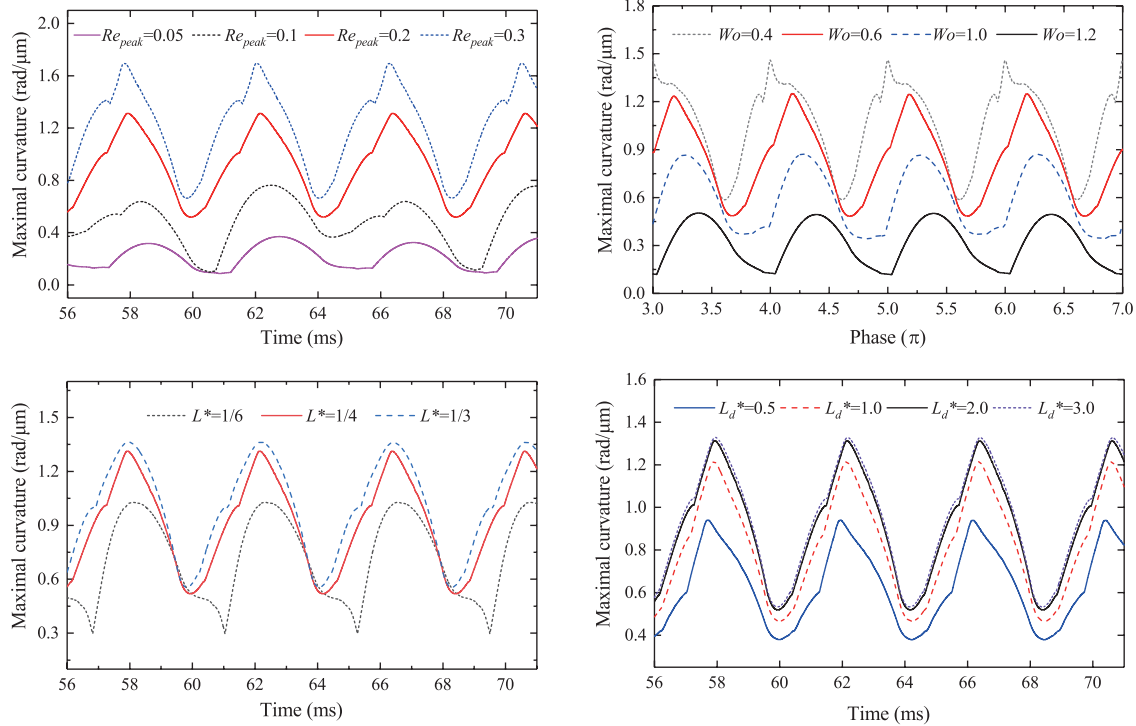**FIG. 4.** Three typical stretch states captured in our simulations.

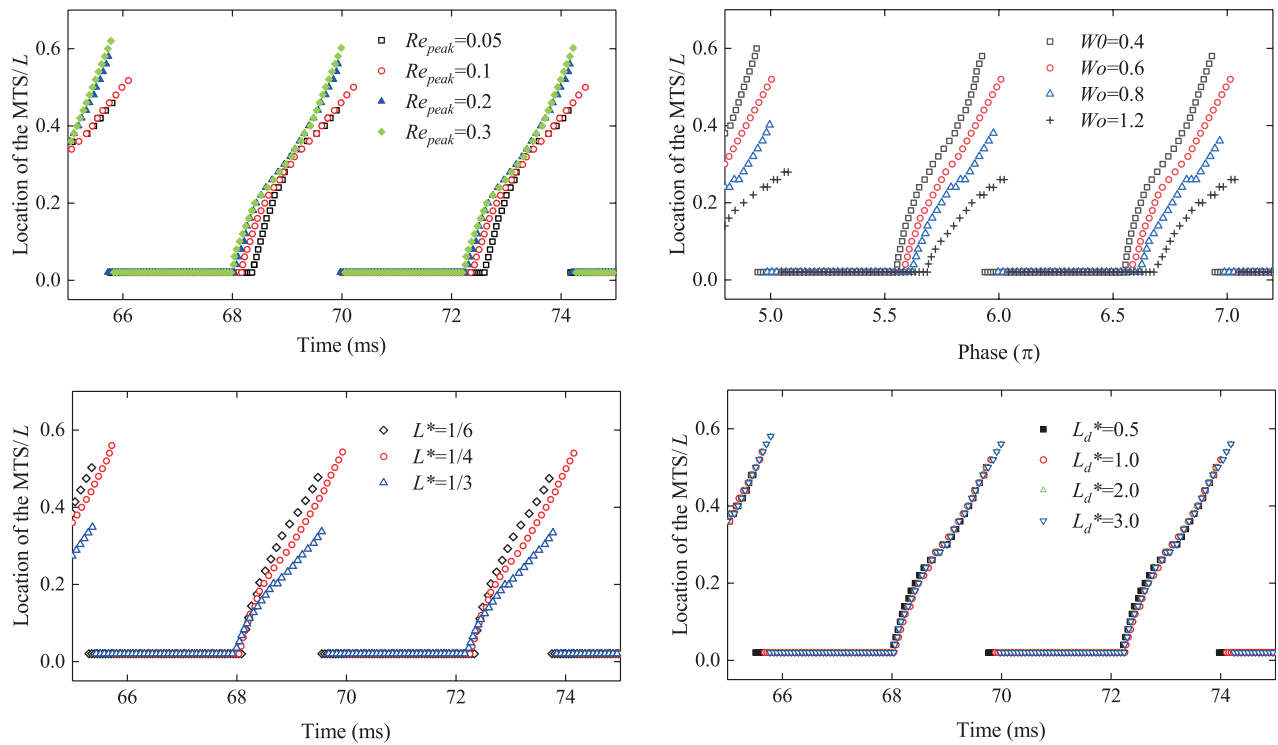**FIG. 5.** Time evolutions of the maximal curvature for various governing parameters.

FIG. 6. Time evolutions of the location of MTS for various governing parameters.

13 January 2025 02:40:17

maximal cilium defection/SD is accompanied by a decrease in the maximal cilium height.

There are three stretch states captured during the cilium deflection process in our simulations, as shown in Fig. 4. In the first stretch state, the direction of the profile curvature (i.e., its principal normal) does not change sign along the cilium length, making one side of the membrane under stretch, while the other side under compression throughout the cilium length (i.e., consistent). In the second stretch state, the direction is observed to change sign once along the cilium length. Consequently, each side of the cilium membrane will be partially under stretch and partially under compression. In the third stretch state, the sign of the direction is found to change twice, and two neighboring sections will be under different stress states. Interestingly, the first and second stretch states are observable in all the simulated cases, while the third stretch state is observed in the case where the long cilium extends into 1/3 of the lumen (i.e., $L^* = 1/3$).

B. Maximal tensile stress (MTS)/curvature

The time evolutions of the maximal curvature for various governing parameters are shown in Fig. 5. The maximal curvature varies periodically with time, and it is found to increase with the Re_{peak}, L^*, and L_d^* (when $L_d^* \leq 2.0$), while decreasing with the Wo. This trend is consistent with that of the maximal deflection. Our previous study[44] suggests that the ciliary deflection and profile curvature lag behind the applied pressure signal. This study further confirms that, according to Fig. 5, this lag behind is even more pronounced at larger Re_{peak} and/or Wo. Figure 6 presents the time evolutions of the location of the maximal tensile stress (MTS) for various governing parameters. Propagation location of the MTS is observed for all the simulated cases, a quite different feature from the steady flow case, where the location is predicted to locate at the cilium's basal end.[45,46] It is also noticed that the propagation does not change considerably when the x-spacing interval is varied. The maximal propagation distance (scaled) as a function of the Re_{peak}, the Wo, the L^*, and the L_d^* is shown, respectively, in Fig. 7, where the maximal deflection is also presented for reference. For a primary cilium with short or medium length, the maximal propagation distance is found to increase with the SD. However, this is not the case for a long primary cilium that protrudes into 1/3 of the lumen, as the arising third stretch state may greatly suppress the propagation location of the MTS [Fig. 7(c)].
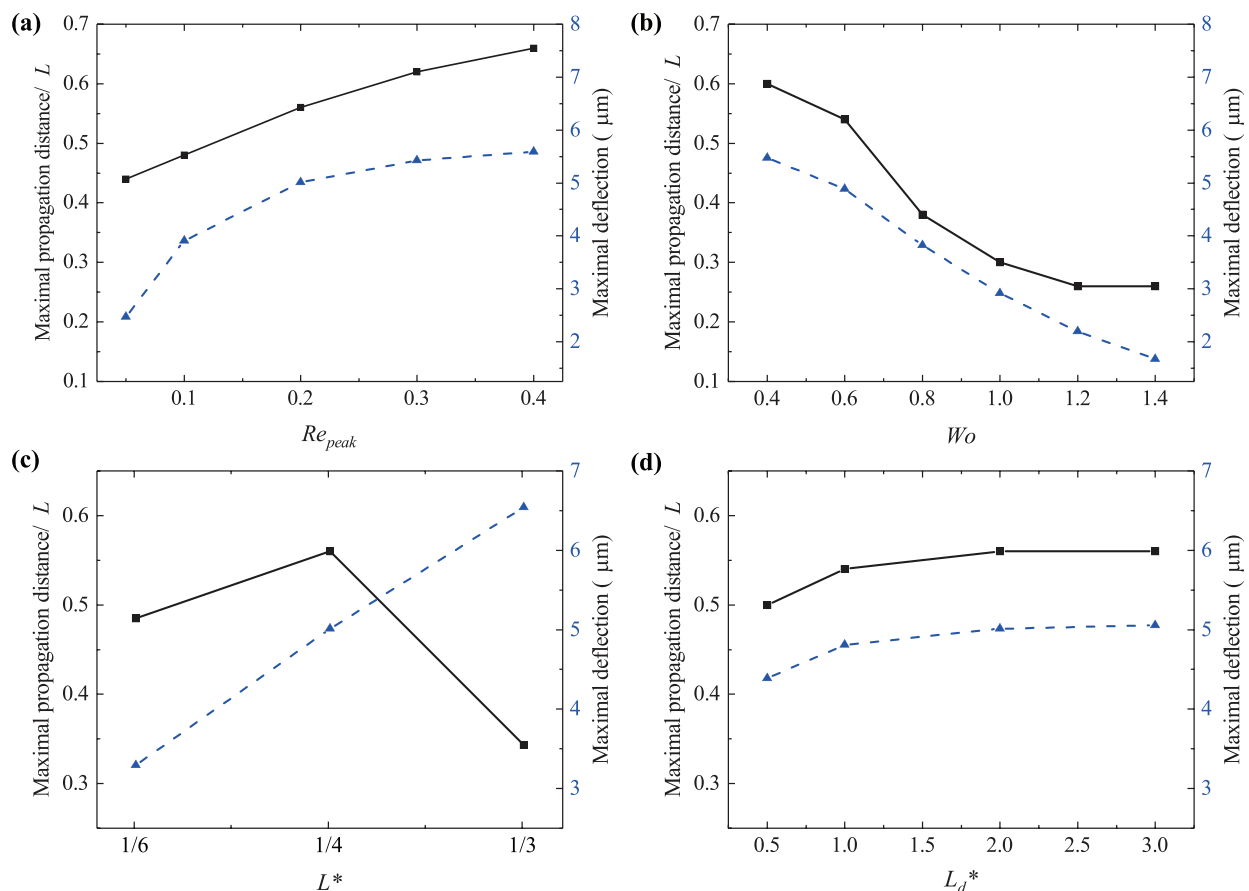
FIG. 7. Maximal propagation distance of the location of the MTS as a function of the (a) Re_{peak}, (b) Wo, (c) L^*, and (d) L_d^*. The dashed blue lines represent the maximal deflection with the scale shown at the right axis.

C. Wall shear stress (WSS)

The WSS is a mechanical stimulus that endothelial cells lining the inner vessel wall are particularly sensitive to. Our previous study[44] suggested that the presence of primary cilia has a considerable impact on the WSS field. The cilia and their flapping motions will decrease the spatial-averaged WSS level and changes the oscillation characteristic of the WSS field by making the WSS in some regions less oscillatory. Here, we further examine if a variation in the considered parameters strengthens or weakens such impact. Figure 8 shows, respectively, the decrease in the average WSS as a function of the Re_{peak}, the Wo, the L^*, and L_d^* (the maximal deflection is also presented for reference). The decrease is evaluated by comparing the time- and spatial-averaged WSS value (in the initial five cycles) between the with and without cilium cases. We can see that, for a fixed L_d^*, the decrease and the maximal deflection share a similar trend, and the decrease is found to be more significant when a cilium undergoes a larger SD [Figs. 8(a)–8(c)]. A more significant decrease in the average WSS can be observed when the L_d^* is reduced, despite that the maximal deflection is almost

unchanged [Fig. 8(d)]. Compared with the x-spacing interval L_d^*, the SD plays a marginal role in decreasing the WSS.

The oscillatory features of the WSS field are evaluated by the oscillatory shear index (OSI), which is defined as[47]

$$\text{OSI} = \frac{1}{2}\left(1 - \frac{\left|\int_0^T \tau_x \, dt\right|}{\int_0^T |\tau_x| \, dt}\right), \qquad (22)$$

where T is the oscillating cycle, and τ_x is the x-component of the WSS vector in the flow direction. The OSI measures the disturbed flow patterns developed that result in the reverse flow velocity components occurring near the vessel walls. The OSI value should be between 0 and 0.5 according to the definition. Zero OSI means a totally unidirectional WSS, while an OSI value of 0.5 denotes a purely unsteady and oscillatory flow with a net amount of zero WSS.

The OSI contours for various governing parameters are presented in Fig. 9. A uniform OSI contour with a value of 0.5 is expected
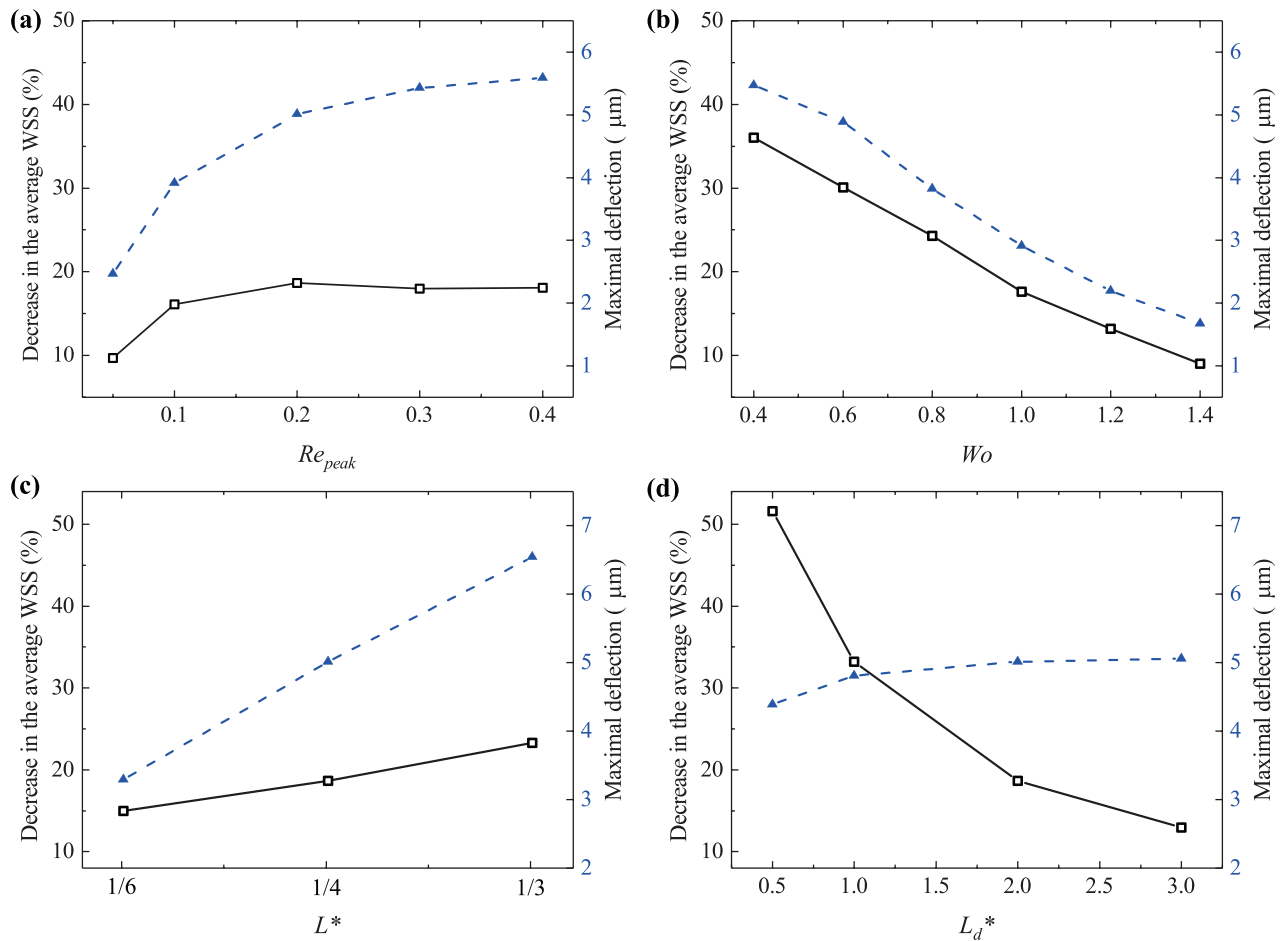
FIG. 8. Decrease in the average WSS as a function of the (a) Re_{peak}, (b) Wo, (c) L^*, and (d) L_d^*. The dashed blue lines represent the maximal deflection with the scale shown at the right axis.

13 January 2025 02:40:17
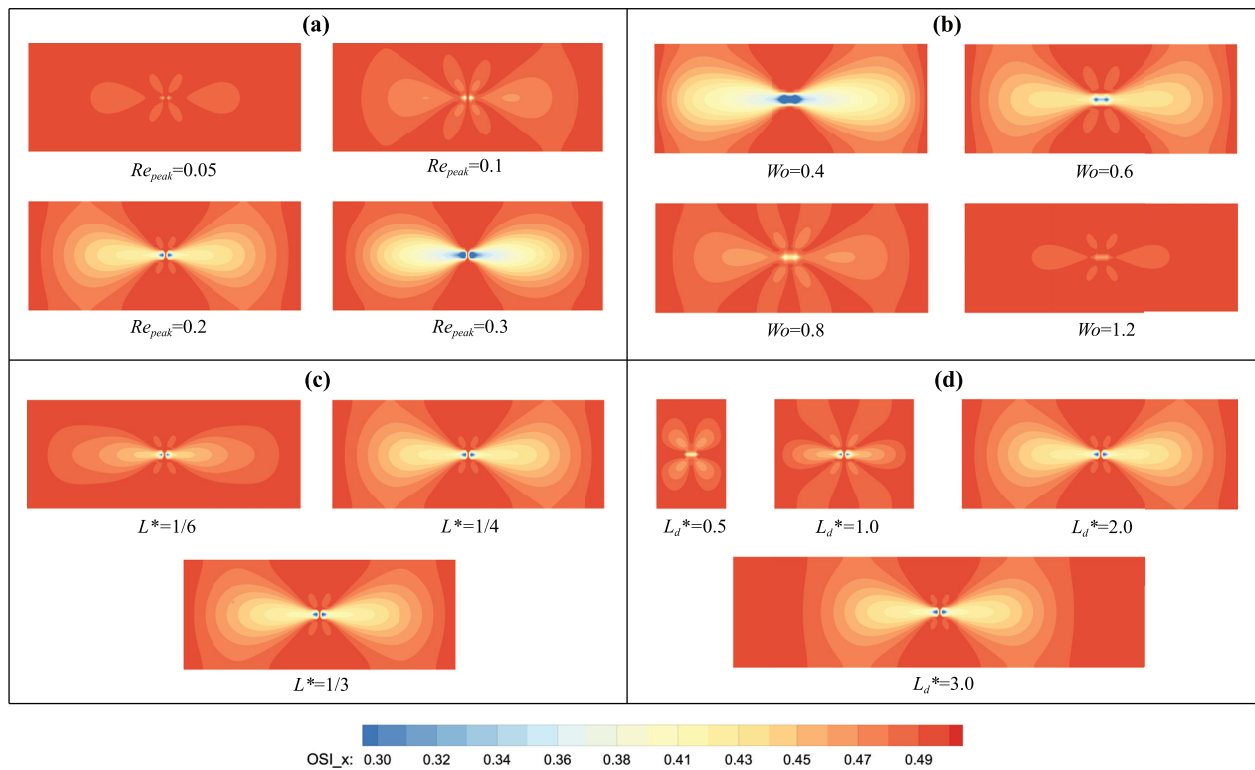
FIG. 9. OSI contours for various governing parameters: (a) Re_{peak}, (b) Wo, (c) L^*, and (d) L_d^*.

when there is no cilium presented as the flow is driven by a sinusoidal pressure gradient signal. In all the cases we simulated, the OSI contour is found to be uneven and vary with space when there is primary cilium. The OSI distribution becomes more uneven as the SD increases [Figs. 9(a)–9(c)], and the shape of the affected (i.e., less oscillatory) region is found to greatly depend on the L_d^* [Fig. 9(d)]. For a sparser cilia array with $L_d^* > 1.0$, there are two evidently less-oscillatory regions observable, which locate in front of and behind the cilium's anchor point, respectively. The cilium's impact on the OSI distribution is found to spread out mainly from the anchor point to those distant areas along the flow direction. When $L_d^* < 2.0$, the two less oscillatory regions in the flow direction start to shrink and become less obvious as L_d^* decreases, while four more less oscillatory regions in the diagonal becomes more evident. The two less oscillatory regions in the flow direction become almost invisible when $L_d^* = 1.0$.

IV. CONCLUSIONS

In this study, numerical investigations are performed with a detailed analysis dedicated to find answers to the questions posed at the beginning. We believed that our results and analysis, to a certain extent, have tentatively answered these questions and lead to a better understanding of the FSI and flow sensing of primary cilia in oscillating fluid flows. However, this does not mean that these questions have completely been resolved or answered, as our current numerical study is still based on a relatively simplified model and only very limited parameter ranges are covered. The major conclusions from our results and analysis are as follows:

(1) Within a certain range, an increase in the Re_{peak}, L^*, and L_d^* is found to bring a larger SD and maximal curvature. An increase in the Wo, however, tends to decrease these two quantities. Compared with the other three parameters, the cilium dynamics is not sensitive to the variation in L_d^*, especially when the spacing interval is greater than twice the cilium length. Increasing the cilium's span of defection decreases its maximal cilium height due to the inextensible condition.

(2) Three stretch states are captured in our simulations by examining the direction of the profile curvature. In the first stretch state, one side of the membrane is stretched, while the other side is compressed throughout the cilium length. In the second stretch state, each side of the cilium membrane will be partially under stretch and partially under compression. In the third stretch state, two neighboring sections will be under different stress states. The first and second stretch states arise in all the simulated cases, while the third stretch state is observed in the long-cilium case with $L^* = 1/3$.

(3) For primary cilia with short or medium lengths, an increase in their maximal tip deflection is accompanied with a greater propagation distance of the location of the MTS. However, this is not the case for long primary cilia that protrude into 1/3 of the lumen, as the arising third stretch state may greatly suppress the propagation.

(4) Our parametric study further confirms that the presence of primary cilia decreases the WSS and changes the oscillating characteristic of the WSS field. The decrease is more significant

when the cilia undergo a larger SD and/or when the L_d^* is reduced. Compared with the L_d^*, the SD plays a marginal role in decreasing the WSS. The shape of the less oscillatory region is found to greatly depend on the L_d^*, and given a constant L_d^*, a larger SD corresponds to a more uneven OSI field.

The results enrich our comprehension on the role of primary cilia as flow sensors and may shed light on the design of artificial flow sensors.

ACKNOWLEDGMENTS

AUTHOR DECLARATIONS
Conflict of Interest

The authors have no conflicts to disclose.

Author Contributions

Jingyu Cui: Conceptualization (equal); Formal analysis (lead); Investigation (lead); Methodology (lead); Writing – original draft (lead); Writing – review & editing (lead). **Yuzhen Jin:** Funding acquisition (equal); Project administration (equal); Resources (equal); Supervision (equal). **Yang Liu:** Conceptualization (equal); Funding acquisition (equal); Supervision (equal); Writing – review & editing (supporting). **Bingmei Fu:** Supervision (supporting); Writing – review & editing (supporting). **Weiwei Yan:** Funding acquisition (supporting); Methodology (supporting); Resources (equal); Writing – review & editing (supporting).

DATA AVAILABILITY

The data that support the findings of this study are available from the corresponding authors upon reasonable request.

REFERENCES

[1]H. Hagiwara *et al.*, "The primary cilia of secretory cells in the human oviduct mucosa," Med. Mol. Morphol. **41**(4), 193–198 (2008).

[2]A. M. Nguyen and C. R. Jacobs, "Emerging role of primary cilia as mechanosensors in osteocytes," Bone **54**(2), 196–204 (2013).

[3]J. R. Davenport and B. K. Yoder, "An incredible decade for the primary cilium: A look at a once-forgotten organelle," Am. J. Physiol.-Renal Physiol. **289**(6), F1159 (2005).

[4]S. M. Nauli *et al.*, "Polycystins 1 and 2 mediate mechanosensation in the primary cilium of kidney cells," Nat. Genet. **33**(2), 129–137 (2003).

[5]H. A. Praetorius *et al.*, "Bending the primary cilium opens Ca2+-sensitive intermediate-conductance K+ channels in MDCK cells," J. Membr. Biol. **191**(3), 193–200 (2003).

[6]H. A. Praetorius and K. R. Spring, "Bending the MDCK cell primary cilium increases intracellular calcium," J. Membr. Biol. **184**(1), 71–79 (2001).

[7]H. A. Praetorius and K. R. Spring, "Removal of the MDCK cell primary cilium abolishes flow sensing," J. Membr. Biol. **191**(1), 69–76 (2003).

[8]S. C. Goetz and K. V. Anderson, "The primary cilium: A signalling centre during vertebrate development," Nat. Rev. Genet. **11**(5), 331–344 (2010).

[9]B. K. Yoder, "Role of primary cilia in the pathogenesis of polycystic kidney disease," J. Am. Soc. Nephrol. **18**(5), 1381–1388 (2007).

[10]B. K. Yoder, X. Y. Hou, and L. M. Guay-Woodford, "The polycystic kidney disease proteins, polycystin-1, polycystin-2, polaris, and cystin, are co-localized in renal cilia," J. Am. Soc. Nephrol. **13**(10), 2508–2516 (2002).

[11]A. I. Masyuk, T. V. Masyuk, and N. F. LaRusso, "Cholangiocyte primary cilia in liver health and disease," Dev. Dyn. **237**(8), 2007–2012 (2008).

[12]S. R. McGlashan *et al.*, "Primary cilia in osteoarthritic chondrocytes: From chondrons to clusters," Dev. Dyn. **237**(8), 2013–2020 (2008).

[13]P. Sen Gupta, N. V. Prodromou, and J. P. Chapple, "Can faulty antennae increase adiposity? The link between cilia proteins and obesity," J. Endocrinol. **203**(3), 327–336 (2009).

[14]N. B. Hassounah, T. A. Bunch, and K. M. McDermott, "Molecular pathways: The role of primary cilia in cancer progression and therapeutics with a focus on hedgehog signaling," Clin. Cancer Res. **18**(9), 2429–2435 (2012).

[15]I. Menzl *et al.*, "Loss of primary cilia occurs early in breast cancer development," Cilia **3**(1), 7 (2014).

[16]T. Y. Besschetnova *et al.*, "Identification of signaling pathways regulating primary cilium length and flow-mediated adaptation," Curr. Biol. **20**(2), 182–187 (2010).

[17]K. Gardner, S. P. Arnoczky, and M. Lavagnino, "Effect of *in vitro* stress-deprivation and cyclic loading on the length of tendon cell cilia *in situ*," J. Orthop. Res. **29**(4), 582–587 (2011).

[18]A. Resnick and U. Hopfer, "Force-response considerations in ciliary mechanosensation," Biophys. J. **93**(4), 1380–1390 (2007).

[19]H. Yin *et al.*, "Mechano-Sensing and shear stress-shielding by endothelial primary cilia: Structure, composition, and function," Biocell **45**(5), 1187–1199 (2021).

[20]Y. C. Lim *et al.*, "Culture and detection of primary cilia in endothelial cell models," Cilia **4**(1), 11 (2015).

[21]M. E. Downs *et al.*, "An experimental and computational analysis of primary cilia deflection under fluid flow," Comput. Methods Biomech. Biomed. Eng. **17**(1), 2–10 (2014).

[22]A. M. Nguyen, Y. N. Young, and C. R. Jacobs, "The primary cilium is a self-adaptable, integrating nexus for mechanical stimuli and cellular signaling," Biol. Open **4**(12), 1733–1738 (2015).

[23]A. Resnick, "Mechanical properties of a primary cilium as measured by resonant oscillation," Biophys. J. **109**(1), 18–25 (2015).

[24]B. S. H. Connell and D. K. P. Yue, "Flapping dynamics of a flag in a uniform stream," J. Fluid Mech. **581**, 33–68 (2007).

[25]L. D. Zhu and C. S. Peskin, "Interaction of two flapping filaments in a flowing soap film," Phys. Fluids **15**(7), 1954–1960 (2003).

[26]P. F. Zhu *et al.*, "Simulation study on the mass transport based on the ciliated dynamic system of the respiratory tract," Comput. Math. Methods Med. **2019**, 6036248 (2019).

[27]X. Zhang, G. He, and X. Zhang, "Fluid–structure interactions of single and dual wall-mounted 2D flexible filaments in a laminar boundary layer," J. Fluids Struct. **92**, 102787 (2020).

[28]S. Tao *et al.*, "A non-iterative immersed boundary-lattice Boltzmann method with boundary condition enforced for fluid-solid flows," Appl. Math. Modell. **76**, 362 (2019).

[29]Q. Huang *et al.*, "Streamline penetration, velocity error, and consequences of the feedback immersed boundary method," Phys. Fluids **34**(9), 097101 (2022).

[30]J. Wu and C. Shu, "Implicit velocity correction-based immersed boundary-lattice Boltzmann method and its applications," J. Comput. Phys. **228**(6), 1963–1979 (2009).

[31]C. Peskin, "The immersed boundary method," Acta Numer. **11**, 479–517 (2002).

[32]H.-Z. Yuan *et al.*, "A momentum exchange-based immersed boundary-lattice Boltzmann method for simulating a flexible filament in an incompressible flow," Comput. Math. Appl. **67**(5), 1039–1056 (2014).

[33]C. S. Peskin, "The fluid dynamics of heart valves: Experimental, theoretical, and computational methods," Annu. Rev. Fluid Mech. **14**(1), 235–259 (1982).

[34]M. Ma, W.-X. Huang, and C.-X. Xu, "A dynamic wall model for large eddy simulation of turbulent flow over complex/moving boundaries based on the immersed boundary method," Phys. Fluids **31**(11), 115101 (2019).

[35]X.-G. Luo, A.-K. Gao, and X.-Y. Lu, "Enhanced performance of a self-propelled flexible plate by a uniform shear flow and mechanism insight," Phys. Fluids **35**(2), 021903 (2023).

[36]R. Wang *et al.*, "Numerical simulations of flow around three cylinders using momentum exchange-based immersed boundary-lattice Boltzmann method," Ocean Eng. **247**, 110706 (2022).

[37]R. Wang *et al.*, "Numerical computations of flow around three equilateral-triangular square cylinders with rounded corners using momentum exchange-based IB-LBM at low Reynolds numbers," Ocean Eng. **263**, 112373 (2022).

[38]D. D'Humières, "Multiple-relaxation-time lattice Boltzmann models in three dimensions," Philos. Trans. R. Soc., A **360**(1792), 437–451 (2002).

[39]L.-S. Luo *et al.*, "Numerics of the lattice Boltzmann method: Effects of collision models on the lattice Boltzmann simulations," Phys. Rev. E **83**(5), 056710 (2011).

[40]K. Premnath and J. Abraham, "Three-dimensional multi-relaxation time (MRT) Lattice–Boltzmann models for multiphase flow," J. Comput. Phys. **224**, 539–559 (2007).

[41]X. He, X. Shan, and G. Doolen, "Discrete Boltzmann equation model for nonideal gases," Phys. Rev. E **57**, R13 (1998).

[42]K. Premnath and J. Abraham, "Lattice Boltzmann simulations of drop-drop interactions in two-phase flows," Int. J. Mod. Phys. C **16**, 25–44 (2005).

[43]J. Cui, Y. Liu, and Y. Jin, "Impact of initial fiber states on different fiber dynamic patterns in the laminar channel flow," Int. J. Mech. Sci. **198**, 106359 (2021).

[44]J. Cui *et al.*, "A three-dimensional simulation of the dynamics of primary cilia in an oscillating flow," Appl. Math. Modell. **108**, 825–839 (2022).

[45]S. Rydholm *et al.*, "Mechanical properties of primary cilia regulate the response to fluid flow," Am. J. Physiol.-Renal Physiol. **298**, F1096–F1102 (2010).

[46]Y.-N. Young, M. Downs, and C. R. Jacobs, "Dynamics of the primary cilium in shear flow," Biophys. J. **104**(2), 152a (2013).

[47]J. E. Moore *et al.*, "Fluid wall shear stress measurements in a model of the human abdominal aorta: Oscillatory behavior and relationship to atherosclerosis," Atherosclerosis **110**(2), 225–240 (1994).

13 January 2025 02:40:17